Research Square

Preprints are preliminary reports that have not undergone peer review.
They should not be considered conclusive, used to inform clinical practice,
or referenced by the media as validated information.

Thermodynamics, kinetics and optical signatures of radiation- related bond-switching defects in As_2X_3 (X = S, Se, Te)

Nikolay Onishchenko

onishchenko.nikolay.msu@gmail.com

The Sarov branch of Lomonosov Moscow State University

Valeria Onishchenko

The Sarov branch of Lomonosov Moscow State University

Research Article

Keywords: Arsenic chalcogenides, Bond switching, Density functional theory, Transition-state theory, Radiation-induced defects, Optical transitions

Posted Date: November 26th, 2026

DOI: https://doi.org/10.21203/rs.3.rs-11669636/v1

License: This work is licensed under a Creative Commons Attribution 4.0 International License.
Read Full License

Additional Declarations: No competing interests reported.

Thermodynamics, kinetics and optical signatures of radiation-related bond-switching defects in As_2X_3 (X = S, Se, Te)

Nikolay Onishchenko, Valeria Onishchenko

Lomonosov Moscow State University Branch in Sarov, Sarov, Russia

Corresponding author: Nikolay I. Onishchenko (onishchenko.nikolay.msu@gmail.com)

Abstract

Radiation-induced bond rearrangements in arsenic chalcogenide glasses can modify their optical response, yet the energetics and recovery kinetics of competing local defect pathways remain poorly quantified. We compare two bond-switching channels in As_2X_3 (X = S, Se, Te): As–X → As–As (channel A) and X–X → As–X (channel B). Hydrogen-terminated cluster models were investigated using density functional theory (B3LYP-D3BJ/def2-SVP), nudged elastic band searches, transition-state and intrinsic reaction coordinate analyses, transition-state theory and time-dependent density functional theory. For As_2S_3, the forward activation barriers are 1.89 eV (A) and 2.43 eV (B). Bond-dissociation-energy estimates obtained with def2-TZVP reproduce the phenomenological switching-energy estimates to within approximately 0.1 eV. For channel A, use of the reverse rather than forward barrier reduces the discrepancy with the experimental defect-recovery timescale from approximately 13 to 2 orders of magnitude. Across S → Se → Te, the isomerization energies exhibit opposite composition trends for the two channels; their predicted recovery times cross between Se and Te. The calculated shift of the first vertical excitation is 0.85–1.00 eV for channel A and increases from 0.99 to 1.47 eV for channel B. These optical shifts are qualitative cluster-level signatures, not direct predictions of an absorption edge. The results identify competing local kinetic and optical responses, while the overall radiation sensitivity remains conditional on defect-generation rates.

Keywords Arsenic chalcogenides · Bond switching · Density functional theory · Transition-state theory · Radiation-induced defects · Optical transitions

1 Introduction

Radiation-induced changes in the optical response of chalcogenide glasses depend on composition and local network structure. Such changes and their bond-switching interpretations have been reported for arsenic-sulfide-based glasses (Shpotyuk et al. 2002) and discussed in broader phenomenological models (Shpotyuk et al. 2019; Shpotyuk et al. 2024). These publications do not, by themselves, establish a universal monotonic ordering of radiation resistance for the three binary glasses As_2S_3, As_2Se_3 and As_2Te_3 examined here. A widely used microscopic framework is the valence-alternation-pair (VAP) model (Kastner et al. 1976), in which bond rearrangement can generate oppositely charged coordination defects, conventionally denoted As^{4+} and X^{1-}. These symbols describe formal coordination-defect states, not atomic partial charges of +4 and −1. Phenomenological models of radiation-induced optical changes (Shpotyuk et al. 2019; Shpotyuk et al. 2024) discuss thermally activated transformations and metastable configurations; quantitative activation barriers are needed to assess the relevance of thermal recovery and possible quantum tunneling.

Cluster-based quantum-chemical calculations of point-defect energetics in As_2S_3 have been reported previously (Dembovskii et al. 1998; Uchino et al. 2000; Simdyankin et al. 2005; Tanaka 2024). However, a systematic comparison of the energy landscape, forward and reverse reaction barriers, and electronic excitation signatures of alternative bond-switching channels across S, Se and Te has not been available within a consistent computational framework.

This work compares the thermodynamics, forward bond-switching kinetics, reverse defect-recovery kinetics, and low-energy electronic-excitation signatures of two structurally distinct local transformations, As–X → As–As (channel A) and X–X → As–X (channel B), in models of As_2S_3, As_2Se_3 and As_2Te_3. We assess possible composition-dependent kinetic effects without identifying a thermal forward rate with the actual rate of defect formation under irradiation.

2 Computational methods

The quantum-chemical calculations were performed with ORCA 6.1 (for the ORCA 6 program family, see Neese 2025). The B3LYP exchange–correlation functional and def2-SVP and def2-TZVP basis sets were employed; the D3 dispersion correction with Becke–Johnson damping (D3BJ) was included for the reaction-path and kinetic calculations. The local atomic environment was represented by hydrogen-terminated molecular clusters: $As_2X_5H_4$ for channel A and $As(HX)_2$–X–XH for channel B. All six composition/pathway combinations were analyzed at B3LYP-D3BJ/def2-SVP for the kinetic calculations. The larger def2-TZVP basis set was used separately to assess the basis-set sensitivity of the thermodynamic energy differences. Equilibrium structures were geometry-optimized using the TightSCF convergence setting and checked for the absence of imaginary vibrational frequencies.

Bond switching was characterized in two distinct ways: the isomerization energy ΔE = E(product) − E(reactant), and a bond-dissociation-energy (BDE) reconstruction, $\Delta E(BDE)$ = BDE(formed bond) − BDE(broken bond), based on five auxiliary molecules for each X and the phenomenological definition used by Shpotyuk et al. (2002). With these conventions, an endothermic isomerization has positive ΔE whereas an energetically unfavorable bond substitution has negative $\Delta E(BDE)$. These quantities have different sign conventions and need not coincide in magnitude because the former also includes relaxation of the entire cluster.

Reaction paths were located by the nudged elastic band (NEB) method with subsequent transition-state optimization (NEB-TS; 10 images). The climbing-image formulation of NEB was described by Henkelman et al. (2000). Refined transition states (TSs) were verified as first-order saddle points by the presence of exactly one imaginary vibrational frequency, and their connectivity to the relevant minima was investigated using intrinsic reaction coordinate (IRC) calculations in both directions. Harmonic vibrational analyses provided zero-point vibrational energy (ZPVE) corrections and Gibbs free energies at 250, 300 and 400 K at B3LYP-D3BJ/def2-SVP.

Thermal rate constants were estimated by conventional transition-state theory (TST; Eyring 1935), and the magnitude of the leading tunneling correction was evaluated using the Wigner approximation:

$$k(T) = \frac{k_B T}{h} exp\left[-\frac{\Delta G\ddagger}{k_B T}\right] \quad (1)$$

$$\kappa(T) = 1 + \frac{1}{24}\left(\frac{hc\nu\ddagger}{k_B T}\right)^2 \quad (2)$$

Here k is the rate constant, T is the absolute temperature, k_B is the Boltzmann constant, h is Planck's constant, $\Delta G\ddagger$ is the Gibbs free energy of activation, κ is the Wigner tunneling correction factor, c is the speed of light, and $|\nu\ddagger|$ is the absolute value of the imaginary transition-state wavenumber (in cm^{-1}). The characteristic time is estimated as $\tau = 1/k$. Unless otherwise indicated, tabulated characteristic times are calculated using classical TST without a tunneling correction.

Vertical electronic excitation energies were calculated using time-dependent density functional theory (TD-DFT) within the Tamm–Dancoff approximation (TDA; 10 excited-state roots, def2-SVP) at the optimized ground-state geometries. We define the decrease in the lowest calculated vertical excitation energy after bond switching as $\Delta E(S_1)$ = E(S_1, reactant) − E(S_1, product); a positive value corresponds to a red shift in excitation energy. This quantity is a qualitative cluster-level descriptor and should not be equated with the measured optical absorption edge of a bulk glass. Atomic charge redistribution was characterized by Löwdin population analysis.

3 Results

3.1 Bond-switching energetics in As_2S_3

For channel A (As–S → As–As), the $As_2S_5H_4$ cluster contains two AsS_3 pyramids sharing a bridging sulfur atom (Fig. 1a). In the product, an As–S bond (2.32 Å) is broken and an As–As bond (2.56 Å) is formed (Fig. 1b), giving a configuration associated with the formal As^{4+}/S^{1-} VAP pair. Channel B (S–S → As–S) starts from an $As(SH)_2$–S–SH cluster containing a homopolar S–S bond (2.10 Å), representing a wrong bond in the network (Fig. 1c). An As–S bond (2.27 Å) forms in the product (Fig. 1d).

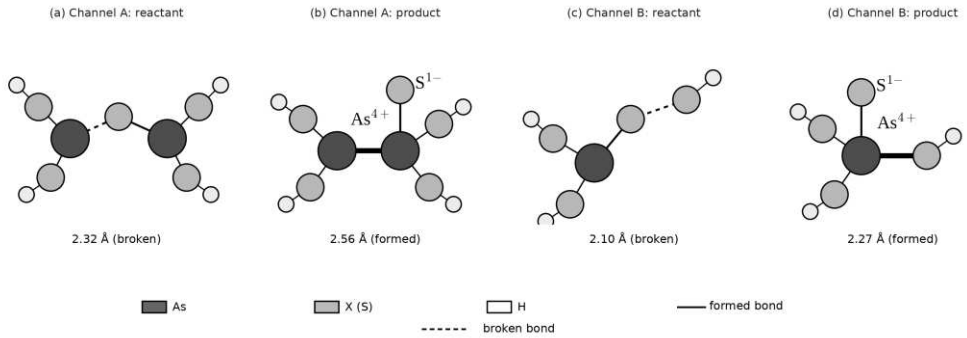

Fig. 1 Hydrogen-terminated cluster models for the two As_2S_3 bond-switching channels. (a, b) Channel A, $As_2S_5H_4$ reactant and product; (c, d) channel B, $As(SH)_2$–S–SH reactant and product. The broken and newly formed bonds are shown by dashed and heavy solid lines, respectively; geometry is schematic

Table 1 compares the calculated switching energies with the phenomenological values of Shpotyuk et al. (2002). The BDE reconstruction reproduces the sign and approximate magnitude of the phenomenological estimate for channel A with both basis sets (differences of 0.10–0.15 eV). For channel B, agreement is obtained only with def2-TZVP: the BDE(As–S)–BDE(S–S) difference is about 0.015 eV with def2-SVP and 0.097 eV with def2-TZVP. This comparison is appropriate for ΔE(BDE), because the phenomenological estimate itself is defined using tabulated bond dissociation energies. In contrast, the isomerization energy measures the cost of fully relaxing the cluster, including regions remote from the switched bond; a systematic difference between these two measures is therefore expected.

Table 1 Bond-switching energy estimates (eV) for As_2S_3: phenomenological reference and present calculations

Level of theory / estimate	Channel A	Channel B
Phenomenological estimate (Shpotyuk et al. 2002)	−0.62	−0.20
Isomerization, def2-SVP	+0.92	+0.39
Isomerization, def2-TZVP	+0.87	+0.47
Isomerization, +D3BJ	+0.87	+0.35
Isomerization, +ZPE	+0.92	+0.40
BDE, def2-SVP	−0.47	+0.02
BDE, def2-TZVP	−0.52	−0.10

3.2 Activation barriers and transition states in As_2S_3

A single first-order TS was located for each channel, with imaginary vibrational wavenumbers of −194.85 cm^{-1} (A) and −323.22 cm^{-1} (B). IRC calculations connected each TS to the corresponding reactant and product minima (Fig. 2). The forward electronic activation energies are 1.89 eV for channel A and 2.43 eV for channel B. The Gibbs free energies of activation vary only weakly over 250–400 K (Table 2), differing from the electronic barriers by at most approximately 0.02 eV, consistent with relatively small net thermal corrections for these particular clusters.

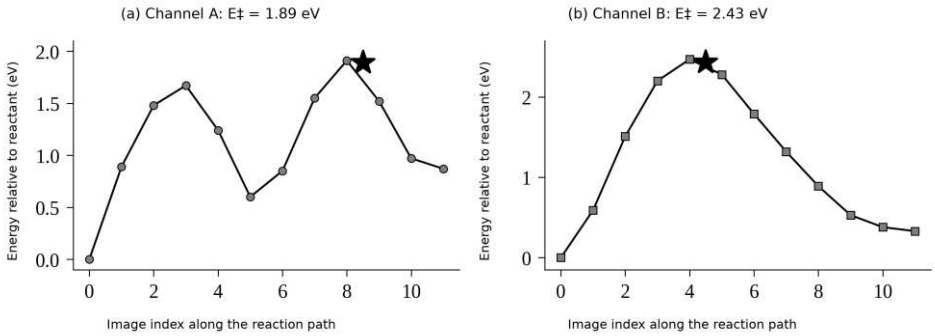

Fig. 2 NEB energy profiles for (a) channel A and (b) channel B in As_2S_3 at B3LYP-D3BJ/def2-SVP. The NEB-TS calculations used 10 images. Stars mark the optimized transition states. The original numerical profiles are retained

Table 2 Gibbs activation free energies ΔG‡ (eV) for forward and reverse reactions in As_2S_3

T (K)	A, forward	A, reverse	B, forward	B, reverse
250	1.885	1.019	2.409	2.047
300	1.889	1.023	2.411	2.049
400	1.899	1.034	2.415	2.055

Classical TST applied to the forward barriers at 300 K gives extremely long formal thermal switching times (Table 3), exceeding by approximately 12–21 orders of magnitude a nominal weeks-to-months post-irradiation relaxation timescale used here for comparison. Studies of irradiation-induced optical relaxation in related chalcogenide glasses provide the broader phenomenological context (Shpotyuk et al. 2019; Shpotyuk et al. 2024), but these works should not be interpreted as direct measurements of the lifetimes of the specific clusters considered here. The contrast is not inherently contradictory: defect generation under ionizing irradiation need not follow the thermally activated forward pathway. The reverse barrier is the more relevant quantity for assessing thermally activated relaxation from an already formed metastable defect.

For channel A, the reverse barrier of 1.02 eV gives $\tau = 6.9$ h at 300 K, roughly two orders of magnitude shorter than the nominal weeks-to-months comparison interval. For channel B, the reverse barrier of 2.05 eV yields $\tau = 1.3 \times 10^{14}$ years, implying negligible thermally activated recovery at room temperature within this cluster model. Thus, for channel A, using the reverse instead of the forward barrier reduces the discrepancy with the adopted timescale from approximately 13 to approximately 2 orders of magnitude. The calculation still gives faster recovery than that benchmark. Increasing the effective reverse barrier by about 0.08–0.15 eV would shift the prediction toward the comparison interval; this difference is not a statistically established uncertainty of the present DFT calculations. The Wigner tunneling factors increase the calculated rates by 1–14% (maximum for channel B at 250 K) and consequently reduce τ, so they cannot remove the discrepancy of this sign.

Table 3 Characteristic times $\tau = 1/k$ at 300 K from classical TST for As_2S_3. Forward times are formal thermal estimates, not radiation-induced defect-generation times

Channel	Forward τ (formal TST)	Reverse τ (recovery)
A	2.7×10^{11} years	6.9 h
B	1.6×10^{20} years	1.3×10^{14} years

3.3 Two-stage reaction pathway for Te, channel A

Unlike the other five composition/channel combinations, the initially found single NEB-TS saddle point for Te/channel A failed to connect the required minima: both IRC branches converged to the reactant. Further analysis indicated a two-step pathway through a shallow intermediate minimum I, 0.04 eV above the reactant (Fig. 3): R → TS1 → I → TS2 → P. Each saddle point has one imaginary vibrational frequency, -109.03 cm^{-1} (TS1) and -125.60 cm^{-1} (TS2). IRC connectivity was unequivocally confirmed for TS2. For TS1 it remains plausible but not fully established, because the small reactant–intermediate energy separation (0.037 eV) led to formal IRC convergence after only a small portion of the path had been traversed.

The apparent rate-controlling saddle differs between reaction directions (Table 4): TS2 lies 1.61 eV above the reactant and controls the forward estimate, whereas TS1 is higher relative to the intermediate for the reverse step (ΔG‡ = 1.23–1.26 eV at 250–400 K, compared with 1.01–1.02 eV for the reverse barrier of step 2). This is the only case among the six examined systems with different apparent limiting TSs in the two directions. Because the reverse estimate for Te/channel A relies on TS1, it inherits additional uncertainty from the unresolved IRC connectivity. Even if step 2 alone controlled the return path (1.01–1.02 eV, $\tau \approx 4$–6 h at 300 K), channel A would still recover more slowly than channel B ($\tau = 53$ s). A full sequential microkinetic treatment would be needed for a quantitatively rigorous overall relaxation time.

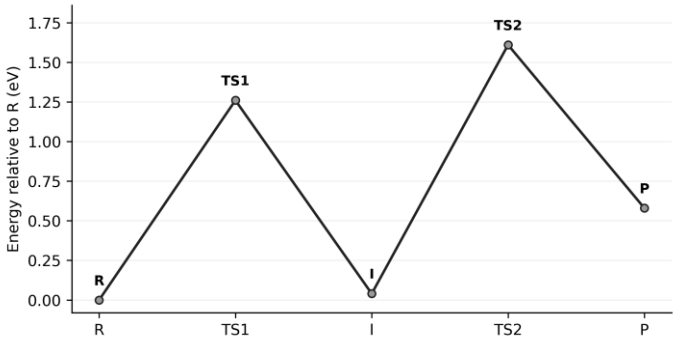

Fig. 3 Schematic two-stage energy landscape for Te/channel A reconstructed from the numerical energies in Table 4: reactant (R), two saddle points (TS1 and TS2), intermediate (I) and product (P)

Table 4 Stationary-point energetics for the two-stage Te/channel A pathway, relative to R

State	E (eV)	Imaginary ν‡ (cm^{-1})
R (reactant)	0.00	—
TS1	1.26	−109.03
I (intermediate)	0.04	—
TS2	1.61	−125.60
P (product)	0.58	—

3.4 Composition trends in activation barriers and recovery kinetics

Table 5 and Figs. 4 and 5 summarize the forward and reverse ΔG‡ values and the associated classical TST times at 300 K. The forward time for channel A varies nonmonotonically with composition, reaching its shortest value for Se (2.2×10^3 years), compared with 2.7×10^{11} years for S and 9.7×10^6 years for Te. The corresponding formal time for channel B decreases monotonically from S to Te: $1.6 \times 10^{20} \rightarrow 6.2 \times 10^{15} \rightarrow 2.1 \times 10^{10}$ years. Channel A is faster than B for forward thermal switching at every composition considered; these formal times do not quantify defect creation under irradiation.

In the reverse direction, channel A is again nonmonotonic: Se recovers most rapidly (6.6 ms), compared with 6.9 h for S and an apparent 3.5 years for Te. Channel B becomes monotonically faster along the chalcogen series, with recovery times of 1.3×10^{14} years, 3.9×10^4 years and 53 s, respectively. The channel order therefore reverses between Se and Te: recovery is faster along A for S and Se, but along B for Te (53 s versus the apparent 3.5 years). The Te/channel A value is a stepwise TST estimate, subject to the TS1 and sequential-kinetics qualifications described in Sect. 3.3.

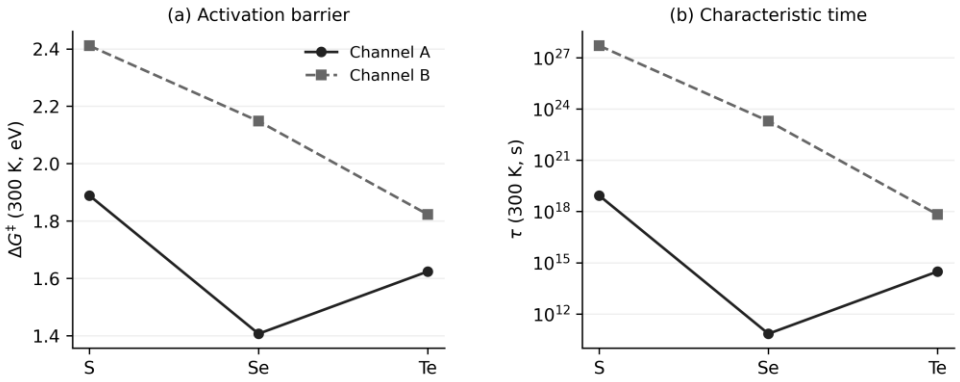

Fig. 4 Forward Gibbs barriers (a) and formal forward characteristic times (b) at 300 K across the S–Se–Te series. Times refer to thermally activated model reactions, not irradiation-driven defect generation

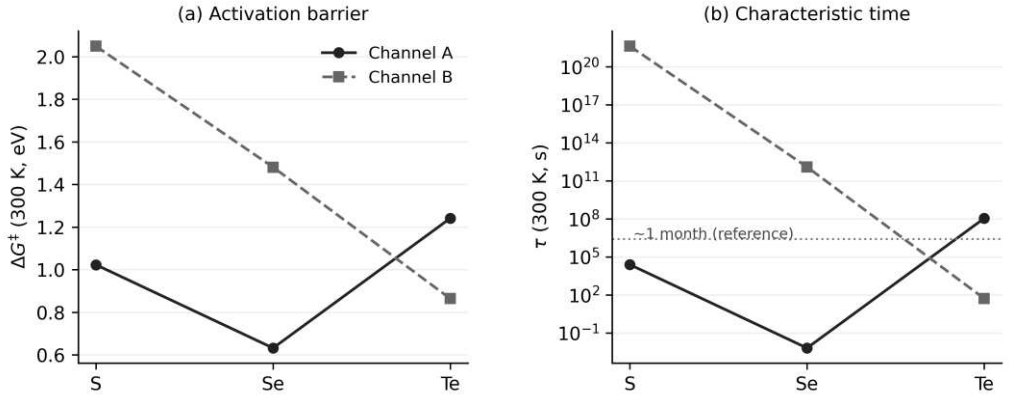

Fig. 5 Reverse Gibbs barriers (a) and recovery characteristic times (b) at 300 K across the S–Se–Te series. For Te/channel A the barrier is the apparent stepwise barrier via TS1, referenced to I; the dotted one-month line is a visual reference, not a fitted experimental dataset

Table 5 Activation free energies ΔG‡ (eV) and classical TST times τ at 300 K across S–Se–Te. Forward τ is a formal thermal estimate; for Te/channel A, the quoted reverse barrier is relative to intermediate I across TS1

Channel	X	ΔG‡ forward	τ forward	ΔG‡ reverse	τ reverse
A	S	1.889	2.7×10^{11} years	1.023	6.9 h
A	Se	1.407	2.2×10^{3} years	0.632	6.6 ms
A	Te	1.624	9.7×10^{6} years	1.241	3.5 years
B	S	2.411	1.6×10^{20} years	2.049	1.3×10^{14} years
B	Se	2.148	6.2×10^{15} years	1.481	3.9×10^{4} years
B	Te	1.823	2.1×10^{10} years	0.864	53 s

3.5 Thermodynamics and optical transition shifts

Table 6 reveals opposite composition trends in the isomerization energies of the two channels (Fig. 6a). Along S → Se → Te, channel A becomes less endothermic (0.92 → 0.85 → 0.67 eV) whereas channel B becomes more endothermic (0.39 → 0.72 → 1.03 eV). For channel A, ΔE(BDE) increases by 0.48 eV (−0.47 → −0.28 → +0.01 eV), consistent with a progressively less costly bond replacement. In channel B, however, ΔE(BDE) changes by only 0.07 eV (+0.02 → +0.06 → +0.09 eV), in the same direction as for A rather than following the isomerization trend (Fig. 6b). This small change is below the 0.12 eV def2-SVP–def2-TZVP difference for the corresponding As_2S_3 value (Table 1). Thus, opposite trends are resolved in total isomerization energies, while the BDE reconstruction supports the trend for A and is inconclusive for B.

The TD-DFT calculations predict positive values of $\Delta E(S_1)$, corresponding to lower first vertical-excitation energies after switching in both channels (Fig. 6c). For channel B, the energy red shift increases from 0.99 eV (S) to 1.19 eV (Se) and 1.47 eV (Te); for channel A, it remains between 0.85 and 1.00 eV. The oscillator strengths of the first transitions are small for some cluster structures (0.004–0.01). These results indicate differences between the calculated low-energy electronic excitations of reactant and product clusters, but do not establish experimentally detectable spectral features, spectral weights, or shifts of the optical absorption edge in bulk glasses.

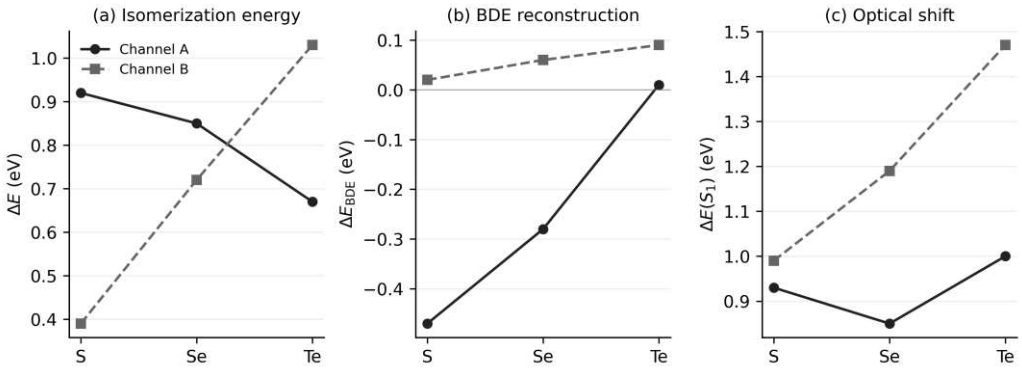

Fig. 6 Isomerization energies (a), bond-dissociation-energy reconstruction ΔE(BDE) (b) and defect-induced first-excitation red shifts (c) for channels A and B across As_2S_3–As_2Se_3–As_2Te_3. Values were reconstructed directly from Table 6

Table 6 Isomerization energies, ΔE(BDE), and TD-DFT first-excitation red shifts $\Delta E(S_1) = E(S_1, \text{reactant}) - E(S_1, \text{product})$ (all in eV)

X	A: ΔE	A: BDE	A: shift	B: ΔE	B: BDE	B: shift
S	+0.92	−0.47	0.93	+0.39	+0.02	0.99
Se	+0.85	−0.28	0.85	+0.72	+0.06	1.19
Te	+0.67	+0.01	1.00	+1.03	+0.09	1.47

3.6 Electronic charge redistribution

Löwdin charges along the reaction coordinate (Table 7) differentiate the two pathways in As_2S_3. In channel A, two initially nearly equivalent As centers (+0.085 and +0.089 in the reactant) acquire different charges at the TS (+0.03 and +0.17), indicating asynchronous redistribution. In channel B, the As charge at the TS (+0.064) is essentially unchanged from the reactant, whereas the sulfur charge has already undergone roughly 60% of its net change (−0.150 within the reactant-to-product interval of −0.039 to −0.223). The saddle point is therefore early with respect to As-charge redistribution but relatively late with respect to S.

For Te/channel A, the Löwdin charge on the bridging chalcogen changes sign between TS1 and TS2: it is +0.112 at TS1, +0.003 at the intervening intermediate I, and −0.237 at TS2. For these same structures in the order TS1 → I → TS2, the two As-center charges are +0.070 → +0.023 → +0.111 and +0.020 → +0.012 → +0.033, respectively. Their unequal changes indicate an asymmetric electronic response; however, these three points do not support a claim of monotonic charge evolution along the full reaction path. The final Löwdin charges at the As_2S_3 defect sites are similar for the two pathways (formal As^{4+} site: +0.126 and +0.132; formal S^{1-} site: −0.216 and −0.223), despite the different mechanisms.

Table 7 Löwdin atomic charges (in units of elementary charge) along the two As_2S_3 reaction coordinates

Site	A: R	A: TS	A: P	B: R	B: TS	B: P
As (formal As^{4+})	+0.085	+0.03 / +0.17	+0.126	+0.064	+0.064	+0.132
S (formal S^{1-})	−0.076	−0.228	−0.216	−0.039	−0.150	−0.223

4 Discussion

The calculations were performed on compact, hydrogen-terminated clusters. This approach allows a consistent comparison of local bond-rearrangement pathways but is not intended to reproduce the absolute barriers of an infinite disordered network, in which cooperative structural relaxation, dielectric screening and the distribution of local environments can alter activation energies. Accordingly, the interpretation emphasizes relative differences between pathways and compositions rather than isolated numerical barriers. Both the B3LYP functional and the cluster size were held fixed, and no systematic convergence tests over these choices were performed.

The trend in channel A is consistent with its bond dissociation energies: the As–As BDE is approximately independent of X (2.07 eV), whereas BDE(As–X) decreases along S → Se → Te (2.54 → 2.35 → 2.06 eV). Replacing As–X with As–As therefore becomes less costly, as suggested by both energy measures. In channel B, BDE(X–X) (2.53 → 2.29 → 1.97 eV) and BDE(As–X) decline similarly by 0.56 and 0.48 eV, respectively, so their difference changes by only 0.07 eV. The 0.64 eV increase in the channel B isomerization energy is therefore not explained by the local difference between the two switched bonds and instead reflects relaxation elsewhere in the cluster.

Although the forward thermal barriers for channel A are lower than those for B for every X, the respective defect-generation rates under irradiation are not determined by these barriers. The irradiation-dependent rates G_A and G_B were not calculated, and no preferred radiolytic generation pathway can therefore be identified. The model does predict a reversal in the relative rates of thermal defect recovery between Se and Te. In a simplified steady-state balance under continuous irradiation, $N_i \sim G_i\tau_i$ for a defect family i; both its generation rate and relaxation lifetime affect its abundance. Quantitative predictions of composition-dependent radiation-induced defect accumulation would require at least G_A/G_B and the populations of relevant defect types. Such information is unavailable here. Moreover, the calculated Se and Te recovery times have not been directly validated against experimental measurements.

From the optical standpoint, both channels lead to lower first vertical-excitation energies in the product clusters, but their trends are distinct. The increasing shift for channel B suggests that this defect family could contribute differentially to composition-dependent sub-gap or near-edge absorption. This is a mechanistic hypothesis rather than an optical-spectrum prediction: absolute transition energies, oscillator strengths across all relevant excited states, disorder broadening, matrix polarization and defect abundances are needed before comparison with measured absorption coefficients or radiation-induced photodarkening. The low oscillator strengths of some S_1 transitions further caution against interpreting a shift in S_1 alone as a shift of an observable bulk absorption onset.

5 Conclusions

Two local bond-switching reactions in models of the arsenic chalcogenides As_2X_3 (X = S, Se, Te) were compared using a consistent DFT and transition-state framework. For As_2S_3, BDE-derived switching energies at def2-TZVP agree with the phenomenological estimates of Shpotyuk et al. (2002) to within approximately 0.1 eV, while calculated forward electronic activation barriers are 1.89 eV (channel A) and 2.43 eV (channel B). For the As–S → As–As pathway, comparison with the reverse rather than the formal forward thermal barrier reduces the discrepancy with the nominal weeks-to-months recovery benchmark from about 13 to about 2 orders of magnitude. Recovery predicted from the cluster reverse barrier remains faster than this benchmark, and the Wigner correction does not resolve the difference.

Across S → Se → Te, the channels exhibit opposite isomerization-energy trends, different composition dependences of the kinetic barriers, and a reversal of their relative stepwise recovery times between Se and Te. Te/channel A involves a two-step pathway with incomplete IRC confirmation for TS1, so its overall relaxation time requires a sequential microkinetic treatment. TD-DFT predicts first-excitation red shifts of 0.85–1.00 eV for channel A and 0.99–1.47 eV for channel B; these remain qualitative optical descriptors of molecular clusters. A quantitative connection to bulk radiation response requires irradiation-dependent defect-generation rates, explicit network-environment effects, and optical-spectrum modeling. Future studies should assess functional and cluster-size sensitivity, dielectric screening, full tunneling corrections, and multi-step reaction kinetics.

References

Dembovskii, S.A., Zyubin, A.S., Grigor'ev, F.V.: Modeling of hypervalent configurations, valence alternation pairs, deformed structure, and properties of a-S and a-As_2S_3. Semiconductors 32, 843–849 (1998). https://doi.org/10.1134/1.1187470

Eyring, H.: The activated complex in chemical reactions. J. Chem. Phys. 3, 107–115 (1935). https://doi.org/10.1063/1.1749604

Henkelman, G., Uberuaga, B.P., Jónsson, H.: A climbing image nudged elastic band method for finding saddle points and minimum energy paths. J. Chem. Phys. 113, 9901–9904 (2000). https://doi.org/10.1063/1.1329672

Kastner, M., Adler, D., Fritzsche, H.: Valence-alternation model for localized gap states in lone-pair semiconductors. Phys. Rev. Lett. 37, 1504–1507 (1976). https://doi.org/10.1103/PhysRevLett.37.1504

Neese, F.: Software update: The ORCA program system—version 6.0. WIREs Comput. Mol. Sci. 15, e70019 (2025). https://doi.org/10.1002/wcms.70019

Shpotyuk, M., Shpotyuk, O., Balitska, V.: Combined configuration-enthalpy model describing radiation-optical responses in chalcogenide semiconductor glasses. Radiat. Phys. Chem. 165, 108401 (2019). https://doi.org/10.1016/j.radphyschem.2019.108401

Shpotyuk, O., Golovchak, R., Kovalskiy, A., Pamukchieva, V., Skordeva, E., Arsova, D.: On the mechanism of radiation-induced optical effects in vitreous As_2S_3–GeS_2. Ukr. J. Phys. Opt. 3(2), 134–143 (2002)

Shpotyuk, O., Vakiv, M., Kovalskiy, A., Golovchak, R., Balitska, V., Shpotyuk, M.: Radiation-induced modification effects in covalent-network glass formers: Phenomenological description within unified configuration-enthalpy model. Appl. Radiat. Isot. 206, 111255 (2024). https://doi.org/10.1016/j.apradiso.2024.111255

Simdyankin, S.I., Niehaus, T.A., Natarajan, G., Frauenheim, T., Elliott, S.R.: New type of charged defect in amorphous chalcogenides. Phys. Rev. Lett. 94, 086401 (2005). https://doi.org/10.1103/PhysRevLett.94.086401

Tanaka, K.: Defects in Se, As_2S_3, and GeS_2 glasses: Ab initio analyses of related clusters. J. Non-Cryst. Solids 633, 122950 (2024). https://doi.org/10.1016/j.jnoncrysol.2024.122950

Uchino, T., Clary, D.C., Elliott, S.R.: Mechanism of photoinduced changes in the structure and optical properties of amorphous As_2S_3. Phys. Rev. Lett. 85, 3305–3308 (2000). https://doi.org/10.1103/PhysRevLett.85.3305

Statements and Declarations

Funding. The authors received no funds, grants, or other financial support for the research reported in this manuscript.

Competing interests. The authors declare that they have no relevant financial or non-financial interests to disclose.

Author contributions. Valeria D. Onishchenko performed the quantum-chemical calculations and generated the computational results. Nikolay I. Onishchenko interpreted the calculations and prepared the manuscript.

Data availability. The numerical values supporting the conclusions are provided in the tables and figures of this article. The original ORCA input and output files have not been deposited in a public repository or supplied as supplementary files with this version of the manuscript.